Cell Reports

Article

A Pushing Mechanism for Microtubule Aster Positioning in a Large Cell Type

Graphical Abstract

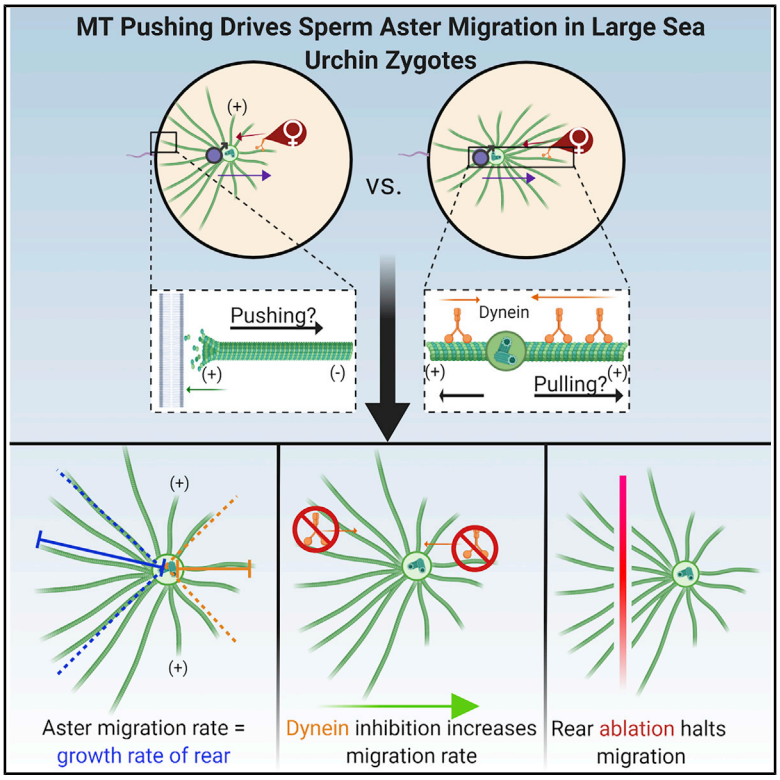

Highlights

- Chemical ablation of rear astral MTs halts aster migration
- Inhibition of dynein-mediated transport increases aster migration rate
- Sperm aster geometry and growth dynamics are consistent with pushing
- After sperm aster centration, the female pronucleus pulls by dynein on the aster

Authors

Johnathan L. Meaders, Salvador N. de Matos, David R. Burgess

Correspondence

david.burgess@bc.edu

In Brief

Meaders et al. demonstrate that a microtubule-based pushing mechanism drives migration and positioning of microtubule asters in the large (~100 μm) sea urchin zygote, a mechanism that was previously thought to be exclusive to small cells due to microtubule buckling and slipping as asters grow to large sizes.

Meaders et al., 2020, Cell Reports *33*, 108213
October 6, 2020
https://doi.org/10.1016/j.celrep.2020.108213

CellPress

Cell Reports

CellPress
OPEN ACCESS

Article

A Pushing Mechanism for Microtubule Aster Positioning in a Large Cell Type

Johnathan L. Meaders,[1,2] Salvador N. de Matos,[1] and David R. Burgess[1,2,3,*]
[1]Department of Biology, Boston College, Chestnut Hill, MA 02467, USA
[2]Marine Biological Laboratory, Woods Hole, MA 02543, USA
[3]Lead Contact
*Correspondence: david.burgess@bc.edu
https://doi.org/10.1016/j.celrep.2020.108213

SUMMARY

After fertilization, microtubule (MT) sperm asters undergo long-range migration to accurately position pronuclei. Due to the large sizes of zygotes, the forces driving aster migration are considered to be from pulling on the astral MTs by dynein, with no significant contribution from pushing forces. Here, we re-investigate the forces responsible for sperm aster centration in sea urchin zygotes. Our quantifications of aster geometry and MT density preclude a pulling mechanism. Manipulation of aster radial lengths and growth rates, combined with quantitative tracking of aster migration dynamics, indicates that aster migration is equal to the length of rear aster radii, supporting a pushing model for centration. We find that dynein inhibition causes an increase in aster migration rates. Finally, ablation of rear astral MTs halts migration, whereas front and side ablations do not. Collectively, our data indicate that a pushing mechanism can drive the migration of asters in a large cell type.

INTRODUCTION

Asters are radial arrays of microtubules (MTs) nucleated from MT organizing centers (MTOCs), such as the centrosome. Accurate positioning of asters is indispensable for central cellular functions during cell division and development. In the zygote, sperm asters nucleate from centrosomes anchored to the male pronucleus and serve a wide range of functions, including uniting the maternal and paternal DNA, providing the centrioles, accurate positioning of the pronuclei, and in some animals targeted delivering organelles and information to precise locations to help establish later cell fate specification (Paix et al., 2011; Reinsch and Gonczy, 1998; Roegiers et al., 1999). Furthermore, during cell division in the embryo, mitotic asters help organize the spindle and deliver cortical signals to dictate the cleavage plane, which subsequently ensures correct partitioning of genetic material into daughter cells (Pollard and O'Shaughnessy, 2019; Rappaport, 1961). Despite its crucial importance to cellular development and function, there are still many gaps in our knowledge of the force balance required for accurate aster positioning.

Mathematical modeling and experimental evidence have supported opposing views for how asters find the correct position in cells of differing shapes and sizes. *In vivo* and *in vitro* evidence indicate that polymerization of MTs against the cell cortex can generate enough force to push their associated MTOCs to the correct position in small cells, such as *Schizosaccharomyces pombe* (Holy et al., 1997; Tran et al., 2001). However, in large cells in which asters often span dozens to several hundreds of microns, pushing forces from MT polymerization against the cortex are thought to be lost due to MT buckling and slipping as MTs become longer (Bjerknes, 1986; Dogterom and Yurke, 1997; Dogterom et al., 2005; Holy et al., 1997). Therefore, large cells, such as sea urchin, frog, and *Caenorhabditis elegans* zygotes, are widely thought to have adopted a pulling mechanism on astral MTs by using the minus end-directed motor protein dynein anchored to the leading cortex (Laan et al., 2012; Nguyen-Ngoc et al., 2007; Saito et al., 2006) or cytoplasmic membranes (Barbosa et al., 2017; Gönczy et al., 1999; Kimura and Kimura, 2011; Kimura and Onami, 2005; Minc et al., 2011; De Simone et al., 2018; Tanimoto et al., 2016, 2018). In this pulling model, retrograde motility of cytoplasmic and/or cortical dynein along astral MTs generates pulling force in the opposite direction. Although dynein-mediated cortical and/or cytoplasmic pulling mechanisms for aster positioning have been extensively studied, there is no evidence in support of a MT-based pushing mechanism in large cell types.

The sperm aster has long served as an instrumental *in vivo* model for studying the positioning of large asters in a cellular and developmental context, due to its long-range movements and opportunity for straightforward manipulation (Bestor and Schatten, 1981; Hamaguchi and Hiramoto, 1986; Harris et al., 1980). The theory that sperm nuclei cannot be pushed to the zygote center due to astral MT buckling and slipping was largely constructed around the radial elongation model for aster growth. In this model, the aster is composed of many long individual MTs that originate from the centrosome (Bergen et al., 1980). However, recent mounting evidence has changed our understanding of MT nucleation, revealing that MTs originate from locations remote from the centrosome in branched (Ishihara et al., 2014,

2016; Murata et al., 2005; Petry et al., 2013; Thawani et al., 2019; Verma and Maresca, 2019) or bundled forms (David et al., 2019). In this updated model for aster growth, pushing forces due to MT polymerization against the cortex may be redistributed among many shorter branched or reinforced bundled MTs, which would prevent buckling and slipping along the cortex. Thus, it is worth revisiting large aster positioning in consideration of the potential for MT polymerization-based pushing forces. Here, we have re-analyzed the question of pushing versus pulling during aster positioning in a large cell type by using the sea urchin zygote, combined with quantitative fixed and live cell confocal imaging, global and local MT manipulation, and dynein inhibition. We found that aster geometry and MT density preclude a MT-length-dependent and cortical pulling mechanism for aster centration. Chemical manipulation of astral MT lengths and growth rates, combined with quantitative tracking of aster migration dynamics, indicates that aster migration is equal to and limited by the length of rear portions of the aster but not correlated with the length of front portions of the aster, providing further support for a pushing rather than a pulling model for sperm aster centration. We also found that rear astral MTs were anchored to the rear cortex, which would antagonize pulling from dynein along front astral MTs. Furthermore, inhibition of dynein caused an increase in aster migration, indicating that it likely represses centration forces rather than contributing to them. Finally, using a light-inducible MT depolymerizing agent, we showed that ablation of rear astral MTs halts aster migration, whereas front and side ablations of astral MTs do not. Collectively, our data indicate that a pushing mechanism can drive the migration of asters in a large cell type.

RESULTS

Sperm Aster Geometry and Density Are Inconsistent with a MT-Length-Dependent and Cortical Pulling Model

Forces may be exerted on the sperm aster from pulling by dynein in the cytoplasm or the cortex, or from pushing by MT polymerization against the cortex. According to a MT-length-dependent cytoplasmic pulling model, the MTs in the front of the aster must be longer than those in the rear (Hamaguchi and Hiramoto, 1986; Kimura and Kimura, 2011; Kimura and Onami, 2005; Tanimoto et al., 2016). Such a length asymmetry is predicted to produce more dynein-dependent pulling forces along the front of the aster relative to the rear, pulling the aster forward. Similarly, in a cortical pulling model, the front of the aster is predicted to be longer than the rear because it must reach the far opposite cortex well before the aster begins moving. Conversely, if rear MTs are pushing the aster to the cell center, aster migration should be limited to the length of the rear portion of the aster and independent of the length of the front. To distinguish between these possible sites of force generation in the sea urchin zygote, we quantified aster geometry and densities using quantitative live-cell and immunofluorescence confocal microscopy during the aster migration phase, which lasts ~15–20 min until centration is complete.

We first performed confocal time-lapse microscopy of live zygotes co-injected with purified EB1-GFP protein to label growing MT plus-ends and purified Tau-mCherry protein, which labels MTs regardless of their dynamic state (Mooney et al., 2017; see Figure S1A and STAR Methods for details). We acquired a single image of Tau-mCherry, followed by a 30-s video of EB1-GFP at 2.5 s per frame at various time points post-fertilization (Figure 1A; Video S1), which minimized photobleaching. At early time points during migration, when the aster has moved only 10 and 15 μm from the point of sperm entry, the average front radius of the aster (Lfront) was not significantly longer than the average rear radius of the aster (Lrear) (Figures 1A and 1B; Video S1). By the time the aster migrated 20–35 μm from the site of sperm entry, Lrear became significantly longer than Lfront (Figures 1A and 1B), which is inconsistent with a MT-length-dependent cytoplasmic pulling model. To provide additional characterization of aster geometry, we repeated a similar analysis (see STAR Methods) on images of Tau-mCherry (Figures S1B and S1C; Video S1). Consistent with our EB1-GFP quantifications, we found that the average Lfront of the aster was not significantly different than Lrear during very early time points post-fertilization when the aster had only migrated 10–15 μm from the point of sperm entry (Figures S1B and S1C). However, the rear portions of the aster become significantly longer than front portions once the aster has migrated 20 μm or farther from the point of sperm entry (Figures S1B and S1C). Last, to obtain length data of the aster in 3D, we fertilized eggs and fixed them in suspension for immunofluorescence confocal microscopy at various time points post-fertilization. We generated maximum intensity projections of z stacks of the entire aster (Figure 1C) by using the same cellular orientation as in our live-cell analysis to ensure top and bottom portions of the aster do not bias our measurements (Figure S1A). Using our defined front and rear region of interests (ROIs), we found that by ~5–10 min post-sperm addition, the rear radius of the aster was longer than the front (Figure 1D).

Asymmetries in aster MT density could also account for a cytoplasmic pulling model. Similar to length asymmetries, a higher density of MTs within the front portion of the aster than in the rear could allow more dynein-dependent pulling forces along the front relative to the rear. To quantify aster densities, we performed average intensity projections of our EB1-GFP time frames, producing an average EB1 density map of the sperm aster. We observed a sharp decrease in mean EB1-GFP intensity between ~2–6 μm from the centrosome (Figure 1E). However, beyond ~6 μm, the aster density became constant throughout the extent of the aster in both front and rear portions (Figure 1E). Furthermore, during all time points after fertilization and at all distances from the centrosome, we found the rear portion of the aster to be denser than the front (Figure 1E). To further quantify aster densities, we repeated the same analysis on our images of Tau-mCherry acquired from the same cells, which produces results comparable to EB1-GFP intensity profiles (Figure S1D). Finally, we performed structured illumination microscopy (SIM) to gain a higher resolution of the density asymmetries of fixed sperm asters. Consistent with fixed confocal and live cell imaging, these super resolution images allowed us to qualitatively observe a much higher density in rear portions of the sperm aster relative to the front (Figure S1E). Hence, the rear radius of the aster is longer and contains more MTs than the front during the rapid migration phase (see below), which is

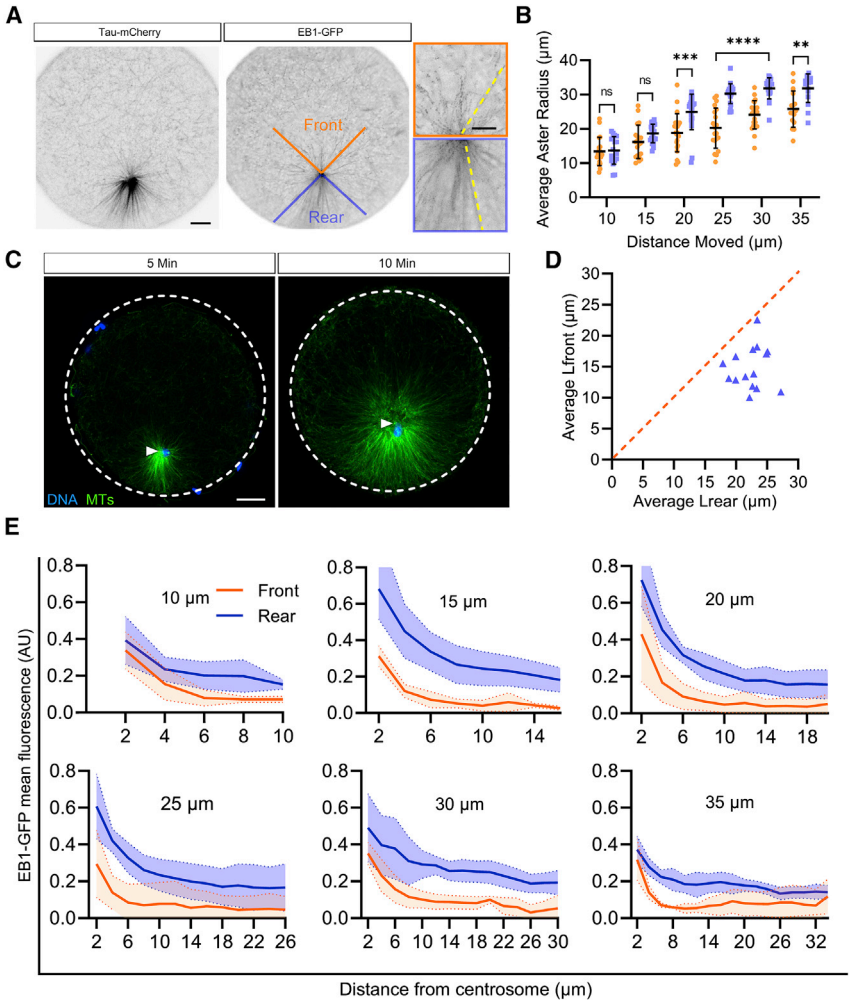

Figure 1. Rear Portions of the Sperm Aster Are Longer and More Dense Than Front Portions

(A) Live-cell confocal microscopy of a zygote co-injected with Tau-mCherry and EB1-GFP. EB1-GFP was imaged for 30 s at 2.5-s intervals, followed by a single frame of Tau-mCherry (see also Video S1). The EB1-GFP channel shown is a single z-slice maximum temporal projection of an aster that has moved 25 μm from the point of sperm entry, which yields quantifiable EB1-GFP tracks (insets) in defined front and rear portions of the aster (see Figure S1A and STAR Methods for more detailed definitions). Measurements of the most distal portion of the EB1-GFP tracks to the centrosomes (dashed yellow lines) were performed to obtain an average length of EB1-GFP tracks in front (orange outline), or cytoplasmic facing side of the aster (defined as Lfront/Front radius, top inset), and the rear, or cortical facing side of the aster (defined as Lrear/Rear radius, bottom inset, blue outlines). Scale bars, 10 μm.

(B) Average maximum aster radius in defined front (Lfront) and rear (Lrear) portions of the aster as described in (A). Each orange circle is the average Lfront of each aster, and each blue square is the average Lrear of each aster (n = 16 zygotes from 5 separate animals). $^{**}p < 0.01$, $^{***}p < 0.001$, $^{****}p < 0.0001$, 2-way ANOVA with Sidak's multiple comparisons. Data represented as mean ± SD.

(C) Representative maximum intensity projections of immunofluorescence z stacks at 5 and 10 min post-sperm addition. Sample orientation is the same as described in Figure S1A, to define front versus rear aster radii. Arrow heads denote the MTOC. Scale bars, 10 μm.

(D) Quantifications of the average maximum Lfront and Lrear of the sperm aster, imaged as in (C). The dashed red line represents a symmetrical aster. n = 15.

(E) Quantifications of average EB1-GFP densities as a function of distance from the MTOC (2-μm intervals) in front and rear portions of the aster at the indicated migration distances (see STAR Methods for additional details). Shaded areas represent ± SD; $p < 0.01$, 2-way ANOVA with Sidak's multiple comparisons, n = 9 zygotes.

See Figure S1 for length/density quantifications based on live Tau-mCherry signal.

inconsistent with a MT-length-dependent cytoplasmic pulling model for aster migration.

Sperm Aster Migration Rates Are Equal to Growth Rates of the Rear Portion of the Aster

We next sought to determine if sperm aster migration distance and/or rates are limited to lengths and growth rates of Lrear. According to the MT-length-dependent cytoplasmic pulling model, the formula $L_{front} - L_{rear}$ was proposed to dictate migration rates, which is thought to account for a constant maximum migration rate regardless of aster size (Tanimoto et al., 2016). Consequently, if aster size is proportionately increased or decreased, aster migration rates should stay the same. Conversely, in a pushing model, aster migration rates will be strictly limited to growth rates of Lrear. To test these hypotheses, we treated cells with ethyl carbamate (urethane) or hexylene glycol (HG) to shorten or lengthen asters, respectively. Urethane was previously shown to shorten astral MTs within the mitotic aster by increasing MT catastrophe (Rappaport and Rappaport, 1984; Strickland et al., 2005), whereas HG increased MT growth rates by decreasing MT catastrophe (Strickland et al., 2005). We found in both live and fixed cells that urethane and HG pretreatment decreased or increased sperm aster diameter, respectively (Figures 2A, 2B, and S2A).

We next measured aster migration rates in urethane-, HG-, and DMSO (control)-treated zygotes by two methods (Figures 2C and S2B). In the first method, which is similar to that of previous studies (Tanimoto et al., 2016), we labeled male and female gamete DNA with Hoechst and tracked male pronuclear movement as a readout for aster migration. Second, to directly detect and track the aster itself, we injected EB1-GFP and tracked aster MTOCs at 5, 10, and 15-min time points after sperm addition, which also allowed us to compare migration rates with growth rates of Lfront and Lrear. In control zygotes, we found that both methods yielded migration rates that were highly consistent with each other, indicating that EB1-GFP injections do not affect

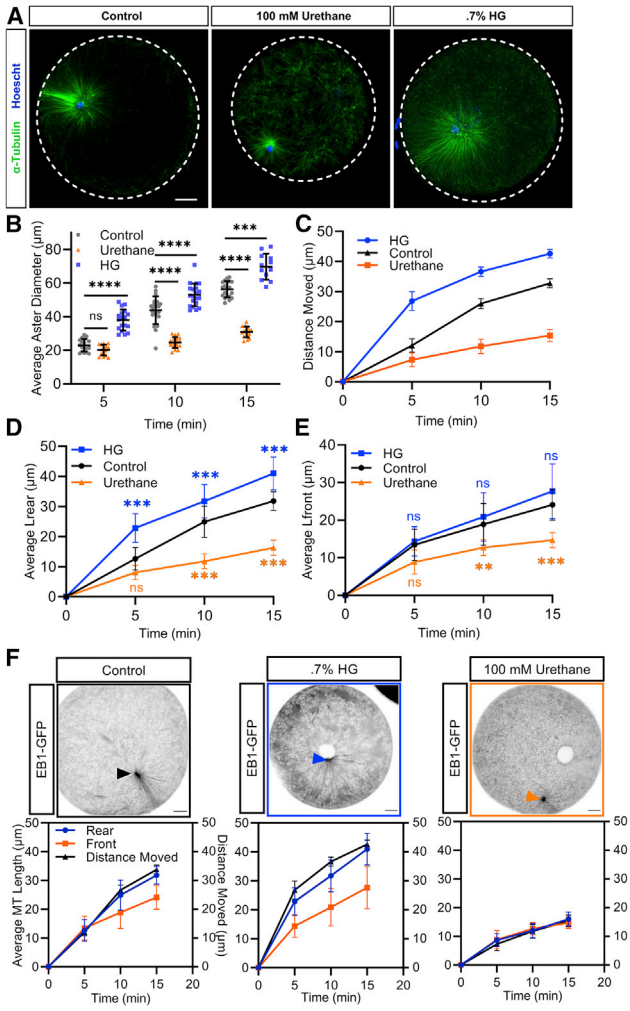

Figure 2. Sperm Aster Migration Rates Scale with Lrear, but Not Lfront, Growth Rates

(A) Representative maximum intensity projections of fixed immunofluorescence z stacks of sperm asters in zygotes treated with urethane to decrease aster size and hexylene glycol (HG) to increase aster size. Asters shown are from zygotes fixed 10 min post-sperm addition. Scale bars, 10 μm.

(B) Quantifications of aster diameters determined by EB1-GFP signal in live embryos imaged for 30 s every 2.5 s at 5, 10, and 15 min post-sperm addition (see also Video S2). Changes in diameter are consistent with quantifications of fixed immunofluorescence z stacks represented in (A) (see Figure S2A for quantifications). ***p < 0.001, ****p < 0.0001; ns, not significant; 2-way ANOVA with Turkey's multiple comparison test. Data represent mean diameter from 10+ zygotes, error bars represent ±SD.

(C) Quantifications of average distance moved, detected by EB1-GFP signal, plotted as a function of time post-sperm addition, (see Video S2), from the site of sperm entry at the indicated time points (see Figures S2B and S2C for further quantifications of aster migration speeds). Lines represent the mean distance moved (n = 8+ zygotes) and error bars represent ±SD.

(D and E) Lfront and Lrear measured by EB1-GFP maximum intensity temporal projections quantified the same as in Figure 1B at 5, 10, and 15-min time points post-sperm addition. Ten-min projections are represented by the images shown in (F). Note that Lrear in HG-treated zygotes expands sooner than Lrear of controls (D). However, Lfront in HG-treated zygotes does not grow faster than controls (E). **p < 0.01, ***p < 0.001, ****p < 0.0001; ns, not significant; 2-way ANOVA with Tukey's multiple comparisons. Lines represent mean Lrear or Lfront calculated from 8+ zygotes from 3 different animals. Error bars represent ±SD.

aster migration (Figure S2B). Additionally, both methods yielded migration rates that were consistent with the three phases of sperm aster migration described by previous studies (Chambers, 1939; Schatten, 1981; Tanimoto et al., 2016; Figure S2B; Video S2). The first is a slow penetration phase just after sperm entry (2.29 ± 0.09 μm/min). The second is the migration phase in which the aster moves most of the distance to the cell center and reaches a constant maximum velocity (4.8 ± 0.2 μm/min). The third is a slow-down phase as the aster nears the cell center and the MTOC becomes bipolar (1.250 ± 0.25 μm/min).

In a pushing model, we predicted that the observed changes in migration rates should scale with changes solely in growth rates of Lrear. To test this hypothesis, we performed a regression analysis comparing changes in average Lfront and Lrear growth rates with changes in average migration rates throughout the three phases of migration in control zygotes (Figure S2C). We found that growth rates of Lrear and migration rates strongly fitted a logistic growth curve (R^2 = 0.80 and 0.98, respectively; $p < 0.001$, comparisons of fit test) (Figure S2C). Conversely, growth rates of Lfront weakly fitted a logistic growth curve (R^2 = 0.51, $p > 0.05$), instead better fitting a linear growth model (Figure S2C). That is, during the first slow phase of aster migration, Lrear grew slowly and matched growth rates of Lfront (Figures 1B, S2B, and S2C), which explains the equal average Lfront and Lrear we observed (Figure 1B). During the second phase, aster migration rates and Lrear growth rates accelerated to a maximum (Figures S2B and S2C). Finally, when the aster slowed down during the third and final stage of migration, Lrear growth rates also decreased as centrosomes separated, forming bipolar asters on each side of the centered male/female pronuclear complex. Conversely, Lfront grew in a slow, more linear fashion, regardless of the phase of aster migration, providing support that migration rates scale specifically with Lrear growth rates (Figure S2C).

In HG-treated zygotes, we found a striking increase in aster migration rates relative to controls (Figure 2C; Video S2). Importantly, asters in HG-treated zygotes displayed increased growth rates of Lrear, but not Lfront relative to controls (Figures 2D and 2E), further confirming that increases in migration rates are dictated solely by growth rates of rear MTs. Furthermore, migration rates closely matched growth rates of only Lrear (but not Lfront) in both control and HG-treated zygotes (Figure 2F). Conversely, in urethane-treated zygotes, the aster was arrested in the first phase of migration in which expansion of Lrear never occurred, resulting in equal Lfront and Lrear (Figures 2C–2F), and asters never accelerated toward the zygote center (Figures 2C and 2F; Video S2). Collectively these data strongly support a pushing model in which aster migration rates are exclusively controlled by growth rates of Lrear rather than a

(F) Comparison of Lfront and Lrear calculated in (D) and (E) with the migration rates calculated in (C), across control, HG-treated, and urethane-treated zygotes. p > 0.05 (ns) comparing distance moved versus Lrear at all time points in all 3 conditions. p < 0.001 (***, highly significant) comparing distance moved versus Lfront at 10- and 15-min time points post-fertilization in control and HG-treated asters. 2-way ANOVA with Tukey's multiple comparisons. Lines are mean from 8+ zygotes, and error bars respresent ±SD. Scale bars, 10 μm. See also Figure S2C and Video S2.

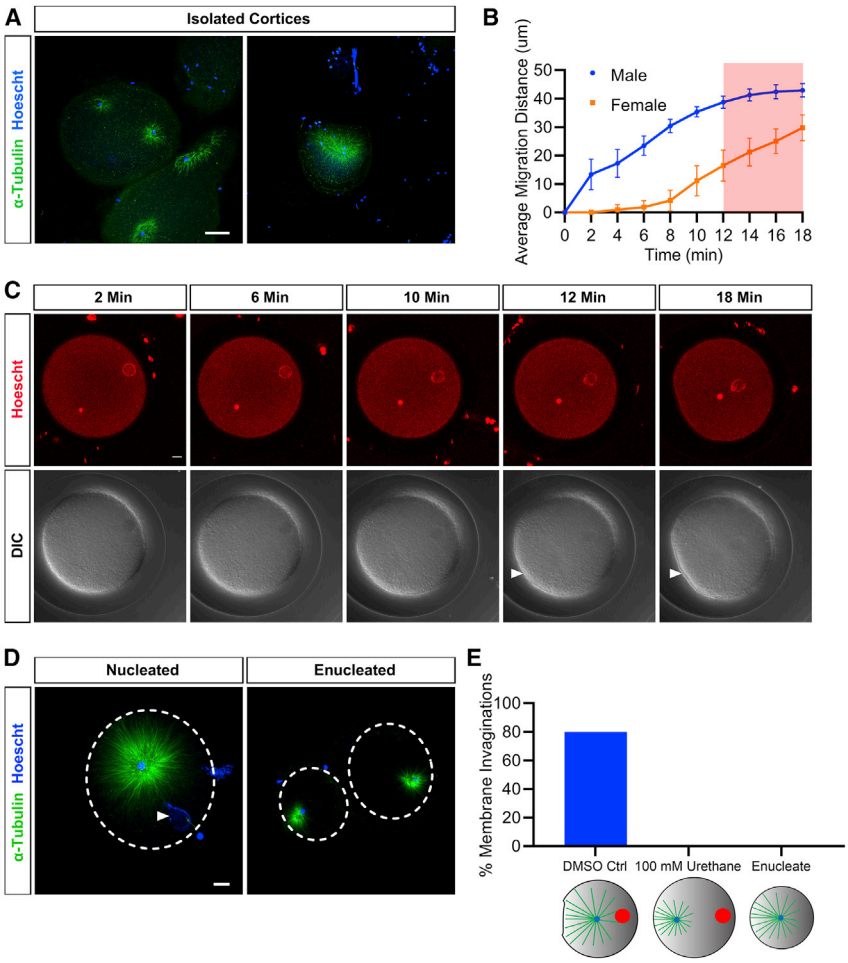

Figure 3. The Sperm Aster Is Anchored to the Rear Cortex

(A) Representative immunofluorescence maximum intensity projections of cortical isolations containing anchored sperm asters. Max projections are ~10 μm thick in z. Scale bars, 10 μm.

(B and C) Live maximum intensity projections and quantification of pronuclear migration dynamics in eggs centrifuged pre-fertilization, which floats the female pronucleus to the cell periphery. Sperm entry in these samples is directly opposite of the female pronucleus. The red region (B) at 12–18 min post sperm-addition indicates when the female pronucleus is being transported along an immobile aster/male pronucleus. Arrow head in (C) annotates rear plasma membrane invaginations on the side of sperm entry during the same time points. See also Video S3. Lines in (B) represent average distance moved at the indicated time point post-fertilization. Error bars represent ±SD, n = 12+ zygotes. Scale bar, 10 μm.

(D) Fixed immunofluorescence 3D projections of sperm asters in centrifuged zygotes. Centrifuging the eggs longer causes them to split, resulting in nucleated and enucleated halves. Arrowhead marks the female pronucleus in a nucleated zygote. Scale bar, 10 μm.

(E) Quantification of zygote rear cortical invaginations as detected in (B) and (C) at 12–18 min post-fertilization. See also Video S3. Schematics illustrate possible pulling force generators on an immobile aster. Note that sperm asters also center in the absence of the female pronucleus (n = 10+ per condition)

pulling model in which migration rates are dictated by the equation $L_{front} - L_{rear}$.

The Sperm Aster Is Anchored to the Rear Cortex

We next aimed to determine whether or not rear astral MTs are also anchored to the rear cortex, which would highlight two key points. The first is that anchoring to the rear cortex should antagonize any potential pulling forces during aster centration. The second is that anchoring of MTs has been shown to prevent MT slipping, as polymerization-induced pushing forces are generated by MTs growing against a surface (Pavin et al., 2012). To explore this question, we used a cortical isolation method commonly used to identify the actin cortex and its interactions with developmental determinants (Burgess and Schroeder, 1977; Henson et al., 2019; Peng and Wikramanayake, 2013). Cortical isolations were prepared ~5–10 min after sperm addition, before dense side and front portions of the aster interact with the cortex (Figure 1C), which means any potential interactions between the aster and the cortex are likely in the rear. In this experiment, we hypothesized that if the aster is not anchored to the actin cortex, it will be washed away with the rest of the zygote cytoplasm during the cortical isolation procedure. Instead, we found full asters including male pronuclei remaining in the cortical preparations (Figure 3A), indicating that the sperm aster is anchored to the rear cortex.

Retrograde Female Pronuclear Transport Exerts Pulling Forces That Are Not Essential for Sperm Aster Centration

In other systems, plasma membrane (PM) indentations or invaginations have been used as a readout for pulling forces on MTs physically coupled to the cell cortex (Negishi et al., 2016; Redemann et al., 2010; Yi et al., 2013). Therefore, we hypothesized that any existing pulling forces on the cortically anchored sperm aster may result in PM invaginations. However, there are two major caveats for detecting potential PM invaginations in our system. The first is that the aster, most notably the rear portion, is rapidly growing during aster migration when potential cytoplasmic pulling forces may be present, which would counteract invaginations of the PM due to pulling from the front portion of the aster. Second, by the time the sperm aster comes to a stop near the zygote center, pronuclear fusion and centrosome separation has usually already occurred resulting in bipolar asters, which are characterized by their own pulling forces to center the zygote nucleus (Minc et al., 2011). To overcome both of these challenges, we designed an experiment in which the

sperm aster approaches the zygote center and halts migration well before engagement, transport, and fusion of the female pronucleus are complete. Unfertilized eggs were centrifuged, resulting in the female pronucleus floating to the centripetal pole (Harvey, 1933). We then fertilized eggs and selected those in which the sperm entry point was at the opposite pole from the female pronucleus for quantitative imaging (Video S3). In fixed samples, sperm aster size and morphology of centrifuged eggs were comparable to those of non-centrifuged eggs, indicating that centrifugation does not affect aster growth (Figures 3D and S3A–S3C). In live centrifuged cells, we found that male and female pronuclear migration occurs in three separate phases (Figures 3B and 3C; Video S3). During the first ~6 min after fertilization, the male pronucleus migrated toward the zygote center in the absence of female pronuclear movement/engagement. Between ~6–12 min post-fertilization, the sperm aster captured the female pronucleus and both pronuclei moved at approximately the same rate toward each other. Finally, during the third phase, the male pronucleus came to a stop near the zygote center, whereas the female pronucleus completed its final migration (Figures 3B and 3C; Video S3). During the third phase, the female pronucleus was transported along a stationary aster, which should have allowed us to detect potential pulling forces. Consistent with this, between ~12–18 min post-fertilization, when engagement between the stationary aster and female pronucleus occurs, the rear membrane displayed a dramatic invagination as the female pronucleus completed its final migration along the stationary sperm aster (Figures 3C and 3E; Video S3). This result further confirms that the sperm aster is anchored to the rear cortex and suggests that pulling forces are present between the male and female pronucleus upon engagement (Figure 3C; Video S3).

The PM invaginations we observed during the last phase of female pronuclear movement could be due to pulling forces from retrograde transport of the female pronucleus, MT-length-dependent cytoplasmic forces, or a combination of both. To distinguish between these possibilities, we repeated the centrifugation experiments in a urethane-treated condition, which results in stationary short asters unable to interact with or capture the female pronucleus (Video S3). We hypothesized that if MT-length-dependent cytoplasmic forces are significant, we should observe PM invaginations in the absence of aster/female pronuclear engagement. In this condition, there were no observable PM invaginations (Figure 3E; Video S3), suggesting that MT-length-dependent cytoplasmic pulling does not substantially contribute the pulling forces required to cause PM invaginations, and the invaginations observed in control centrifuged eggs are instead due to pulling by retrograde transport of the female pronucleus.

To further investigate this point, we tested pulling forces in the complete absence of the female pronucleus, enabling us to directly determine if pulling forces other than those from engagement between the male and female pronuclei contribute to the dimpling we observe. To this end, we centrifuged eggs slightly longer and at a higher speed to split them into two cells, resulting in nucleated and enucleated halves. Both halves can be fertilized and develop to the pluteus larval stage (Harvey, 1933). When we fertilized enucleated halves, we observed smaller asters that displayed a front:rear aspect ratio comparable to that of full-sized cells. This indicates that although smaller enucleated eggs resulted in smaller asters, the shape of these smaller asters was not affected (Figures S3A and S3B). More importantly, enucleated halves displayed normal sperm aster centration (Figure S3A; Video S3C), confirming that potential pulling forces from the female pronucleus were non-essential to aster migration (Figure 3D; Video S3C). Furthermore, in centered, stationary asters of enucleated zygotes, we did not observe any membrane invaginations, indicating that the engagement between the male and female pronuclei provided the pulling force seen in nucleated eggs (Figures 3D and 3E; Video S3). We conclude that retrograde transport of the female pronucleus generates substantial pulling forces on the sperm aster, which are non-essential for most sperm aster migration as the aster centers normally in enucleated eggs. Moreover, there was no detectable contribution of MT-length-dependent cytoplasmic pulling forces to these indentations.

Inhibition of Dynein-Dependent Retrograde Transport Results in Faster Aster Migration Rates

The lack of essential cytoplasmic pulling forces detected in this system prompted us to revisit the requirement for dynein during aster positioning. The cytoplasmic dynein inhibitor ciliobrevin was previously used to stop dynein activity and male pronuclear migration (as a readout for aster migration) in sea urchins, an experiment integral to the MT-length-dependent cytoplasmic pulling model (Tanimoto et al., 2016). However, cytoplasmic dynein has been strongly implicated in focusing of MTs to centrosomes (Goshima et al., 2005; Merdes et al., 2000). Additionally, ciliobrevins have been shown to inhibit spindle pole focusing (Firestone et al., 2012). Because the specificity of ciliobrevin, a general AAA ATPase inhibitor, for dynein is also in question (Roossien et al., 2015), we carefully analyzed the effects of ciliobrevin on sperm asters. We observed sperm aster integrity by using live and fixed-cell immunofluorescence microscopy in ciliobrevin-treated zygotes. Ciliobrevin was added to cells 5 min post-fertilization to ensure there was sufficient time for the aster to expand. We used 100 μM and 50 μM, which were the concentrations previously used to purportedly inhibit aster migration in sea urchins (Tanimoto et al., 2016, 2018). By immunofluorescence, we found that a 5-min treatment with 100 μM of ciliobrevin completely abolished asters (Figure 4). At 50 μM ciliobrevin, aster MTs were almost completely disassembled (Figure 4). Following MTs in live cells with injected Tau-mCherry, disruption of aster morphology became apparent at ~125 s after ciliobrevin addition (Figure 4B; Video S5). These cells displayed signs of MT disassembly in both rear and front portions of the aster, followed by complete disintegration of the aster by 10 min. These data indicate that the previously reported halt in male pronuclear migration seen after ciliobrevin treatment (Tanimoto et al., 2016) may not be due to inhibiting dynein-dependent MT-length-dependent cytoplasmic pulling forces along the associated aster. Instead, the observed halt of the male pronucleus may be because there is no longer an aster to provide centration forces.

To assess the requirement of dynein more directly during aster migration in sea urchin zygotes, we used a more specific method

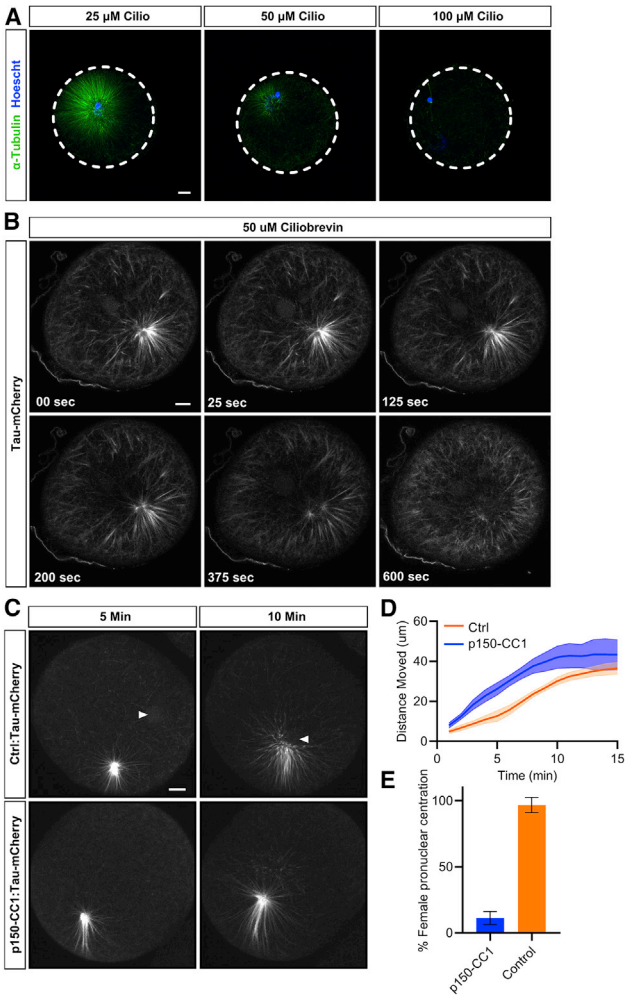

Figure 4. Dynein Inhibition with p150-CC1 Prevents Capture/Transport of the Female Pronucleus and Increases Aster Migration Rates

(A) Representative immunofluorescence maximum intensity projections of sperm asters in zygotes treated with different concentrations of the dynein inhibitor ciliobrevin D. Scale bar, 10 μm.

(B) Live-cell confocal time series of sperm asters labeled with Tau-mCherry and treated with 50 μM of ciliobrevin. Drug was added at time point 0. See also Video S4. Scale bar, 10 μm.

(C) Live-cell confocal images of cells injected with only Tau-mCherry or co-injected with Tau-mCherry and p150-CC1 to inhibit dynein. See also Video S5. Arrowhead marks the female pronucleus in controls. Scale bar, 10 μm.

(D) Quantifications of aster migration distance as a function of time post-fertilization from videos acquired in (C). Solid lines represent the average distance moved in each condition, and shaded areas represent ±SD (n = 11 zygotes per condition). Distance moved is significantly different between conditions from 1–9 min ($p < 0.05$). Notably, 9–15 min is not significantly different; 2-way ANOVA with Sidak's multiple comparisons.

(E) Average percentage of zygotes in which the female pronucleus undergoes retrograde transport along the sperm aster to the cell center in p150-CC1-injected and control zygotes imaged as in (C). n = 11 zygotes per condition from 3 separate animals, Error bars represent ±SD.

to inhibit dynein. To this end, we co-injected eggs with Tau-mCherry and a p150-CC1 fragment, which functions through dominant-negative disruption of the dynactin/dynein interaction to inhibit cytoplasmic dynein (Quintyne et al., 1999). Surprisingly, we found that sperm asters in p150-CC1-injected zygotes migrated to the cell center at faster rates than controls injected only with Tau-mCherry (Figures 4C and 4D; Video S5). We also found that in some cases, asters began rotating in the egg, revealing spiral shapes as they neared the cell center (Video S5). To determine if the level of dynein disruption is sufficient to stop retrograde transport in p150-CC1 injected eggs, we quantified the percentage of microinjected zygotes in which the female pronucleus reached the cell center, which is likely due to dynein-dependent transport along the sperm aster, as shown in other systems (Reinsch and Karsenti, 1997). We found that only 11.3% of p150-CC1-injected zygotes contain centrally located female pronuclei, whereas 96% of controls contain centrally located nuclei 20 min after sperm addition (Figures 4C and 4E; Video S5), indicating that cytoplasmic dynein is sufficiently disrupted to prevent retrograde cytoplasmic transport of the female pronucleus along astral MTs. Finally, because p150-CC1 injections were performed before fertilization, dynein was inhibited at each of the three stages of sperm aster migration, indicating that that pulling forces from dynein-dependent retrograde transport are not essential for any stage of aster migration. We conclude that although dynein activity is required for engagement and retrograde transport of the female pronucleus along the sperm aster, it may instead function antagonistically to centration forces acting on the sperm aster, as indicated by increased migration rates in the presence of p150-CC1.

The Sperm Aster Is Pushed to the Zygote Center by Rear MTs

As a final, more direct approach to testing the contribution of pushing versus pulling forces during aster centration, we sought to ablate the rear portion of the aster and directly follow aster migration dynamics using the Tau-mCherry MT label (Mooney et al., 2017). A long-standing hypothesis proposes that ablation of rear astral MTs will stop aster migration if pushing is predominant (Reinsch and Gonczy, 1998). Conversely, if aster migration is driven by pulling forces that scale with the length of front MTs, rear ablation should increase migration rates by increasing Lfront relative to Lrear (Reinsch and Gonczy, 1998). Laser ablation of the rear astral MTs is not feasible because it disrupts the rear cell membrane in the sea urchin zygote (Tanimoto and Minc, 2017). Therefore, we instead used targeted chemical ablation of MTs with the light-inducible MT-depolymerizing compound caged-combretastatin 4A (CA4) (Costache et al., 2017; Wühr et al., 2010). We activated a low dose of CA4 between ~4–8 min after sperm addition in a rectangular region of the rear sperm aster, proximal to the rear cortex (Figure 5A; Video S6). We observed depolymerization of the dense rear MTs near the cortex after the UV pulse (Figures 5A and 5B; Video S6). Sperm aster migration came to a stop almost immediately after rear UV-activation, well before it reached the zygote center (Figures 5A–5C; Video S6). Conversely, ablation of front or side portions of the aster did not halt aster migration (Figure 5C; Video S7). However, side ablations did cause the sperm aster to drift away from

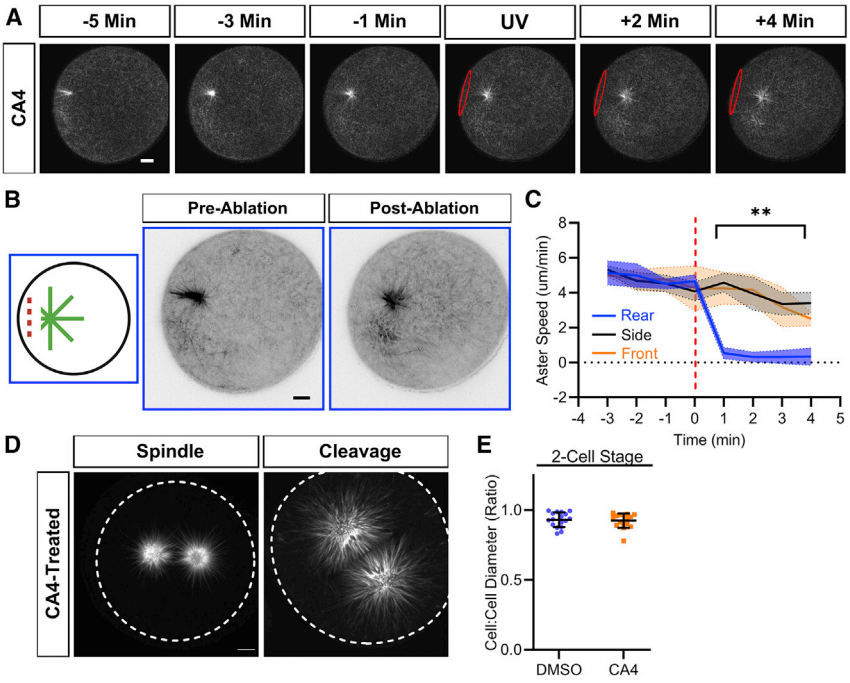

Figure 5. The Sperm Aster Is Pushed to the Zygote Center by Rear Astral MTs

(A) Confocal time-lapse images of Tau-mCherry-injected zygotes treated with the light-inducible MT inhibitor CA4. A region of the rear astral MTs was irradiated with UV light (outlined in red). Scale bars, 10 μm.

(B) Maximum temporal projections of a sperm aster before and after activation of CA4 in the rear portion. Note the loss of rear astral MTs after CA4 activation. The approximate regions of UV activation are indicated in the left illustration. Gray-scale LUTs were inverted to detect aster mass loss more easily. See also Video S6 and Figure S4A. Scale bar, 10 μm.

(C) Quantifications of average aster speed as a function of time before and after ablation of rear, side, and front portions of the sperm aster. The red dashed line indicates the ablation time point. See also Videos S6 and S7. Solid lines represent the mean, and shaded regions represent ±SD (n = 6 per condition). **p < 0.001 comparing rear versus side and rear versus front; 2-way ANOVA with Sidak's multiple comparisons test.

(D) Live-cell images of spindle formation and cleavage in Tau-mCherry-injected embryos treated with CA4. Without UV activation of CA4, cells form robust spindles, which proceed to equatorial cleavage. The future cleavage plane can be determined by the mid zone between anaphase asters where tubulin signal is not present.

(E) Quantification of cell diameter in the 2-cell embryo. The cell:cell ratio is the diameter ratio of each of the two cells. Note in both conditions, the ratio very close to 1.0 indicates that each of the two cells are approximately equal diameter as a result of equatorial division. p < 0.7336 (ns), Unpaired t test. Error bars represent ±SD (n = 17 per condition).

the side of ablation, which suggests a role in guiding the aster (Video S7). Observation of aster depolymerization in front and side portions of the sperm aster were more difficult to detect with maximum temporal projections, which is likely due to the movement of the sperm aster through the region of ablation (Figure S4A). Before UV uncaging, aster migration rates in CA4-treated zygotes were ~4.8 μm/min, which is comparable to aster migration rates in untreated zygotes (Figure S2A; Figure 5C), indicating that the caged compound is not affecting aster migration rates in unintended ways. Additionally, cells treated with CA4 without UV activation displayed normal spindles and equatorial division, further controlling for unintended effects of CA4 on MT organization (Figures 5D and 5E). Together, these data provide direct support that pushing from rear MT growth drives sperm aster migration and rule out any significant contribution from cytoplasmic pulling forces that scale with MT length.

DISCUSSION

Correct positioning of MT asters is vital to cellular development and function. Hence, the nature of the force mechanism responsible for MT aster positioning represents an important question in cell and developmental biology. Elaborate studies of large mitotic asters in zebrafish and *C. elegans* embryos have elucidated cortical and cytoplasmic dynein-dependent pulling mechanisms (Kozlowski et al., 2007; Wühr et al., 2010). However, *in vivo* studies of sperm aster migration are notably limited to work in *C. elegans* (Barbosa et al., 2017; Gönczy et al., 1999; Nguyen-Ngoc et al., 2007; De Simone et al., 2018), which convincingly indicates that the sperm aster/pronuclear complex is predominantly pulled to the zygote center by dynein-dependent forces. Furthermore, a wealth of *in vitro* and *in silico* data indicate pushing during large aster migration is unlikely (Bjerknes, 1986; Dogterom and Yurke, 1997; Holy et al., 1997). Thus, a pushing mechanism for large aster positioning has not been identified. Here, we reveal a long-ranged MT-based pushing mechanism responsible for sperm aster centration in the sea urchin zygote.

Our findings contrast with the previously proposed cytoplasmic MT-length-dependent pulling model in the sea urchin system (Hamaguchi and Hiramoto, 1986; Tanimoto et al., 2016). First, the pulling model is dependent on a longer front aster radius than the rear. However, we found the exact opposite, with Lrear being substantially longer than Lfront during the second, rapid migration phase and the third phase of aster migration (Figures 1A, 1B, S1B, and S1C). These findings are consistent with earlier observations of aster asymmetry in the sea urchin (Chambers, 1939) and yet are inconsistent with more recent work in support for a MT-length-dependent pulling model (Tanimoto et al., 2016). One potential explanation for the inconsistencies between our result and recent work is a difference in the point of reference when performing aster length measurements. Measurements performed by Tanimoto et al. (2016) used the male pronucleus to estimate the location of the MTOC. As such, their study measures the aster radius in front and rear portions of the aster from the male pronucleus. Conversely, in our live and fixed-cell imaging, we performed our measurements from the MTOC itself, which is located in front

of the nucleus soon after fertilization (Figure 1C; Video S1). Our observation that the MTOC is located in front of the male pronucleus is consistent with work using electron microscopy, which shows that the MTOC rotates to the front of the male pronucleus prior to aster formation (Longo and Anderson, 1968). Because Tanimoto et al. (2016) measured from the male pronucleus, which ranges from ~5–8 μm in length, these quantifications simultaneously over- and under-represent front and rear lengths of the aster, respectively. This over/under-representation of front/rear aster radii likely accounts for their conclusion that the aster front radius is 5–10 μm longer than the rear (Tanimoto et al., 2016). Finally, one decisive advantage of our aster length measurements over previous quantifications is that we further support our measurements by imaging the aster in living cells. Such live cell imaging obviates potential artifacts of fixing MTs and pronuclei for immunofluorescence.

Second, experimental support for dynein's role in the cytoplasmic length-dependent pulling model was entirely based on the use of ciliobrevin, assuming that its only effect was on dynein (Sallé et al., 2018; Tanimoto et al., 2016, 2018). We found that ciliobrevin completely abolished aster integrity, precluding interpretations of its effects on dynein's role during sperm aster migration (Figures 4A and 4B; Video S4). Indeed, the degree of specificity of ciliobrevin for dynein inhibition is unclear (Roossien et al., 2015), raising significant concerns about any results attributing its effects on aster migration to dynein inhibition. By inhibiting dynein specifically through p150-CC1 fragment injections, our work indicated that dynein may instead be functioning antagonistically to centration forces in the sea urchin sperm aster. That is, sperm asters center at a higher migration rate in p150-CC1-injected cells (Figures 4C–4E; Video S5). Therefore, our results indicate that retrograde transport by cytoplasmic dynein is more likely antagonistic to aster centration in sea urchin zygotes.

What is the exact role(s) for dynein during aster migration in the sea urchin? Although we speculate more on the role of cortical and cytoplasmic dynein below, our study demonstrated with the use of p150-CC1 injection that cytoplasmic dynein is required for engagement and retrograde transport of the female pronucleus along the sperm aster. A role for dynein during female pronuclear capture and transport has been well studied in other systems (Gönczy et al., 1999; Payne et al., 2003; Reinsch and Karsenti, 1997). However, outside the use of ciliobrevin, which causes a loss of the sperm aster (Figures 4A and 4B), a role for dynein during female pronuclear capture and transport has not been investigated in the sea urchin system prior to this study. We also demonstrated that although this transport provides pulling forces on the aster, it is neither essential for centration (Video S3; Figure S3A), nor is it guaranteed that this transport will happen on the front of the aster where centering pulling forces must occur in a MT-length-dependent cytoplasmic pulling model. That is, female pronuclear engagement and subsequent transport along the sperm aster occurs at locations and time points that are dependent on where the sperm enters the egg relative to the female pronucleus. If the egg is fertilized at a location in which the female pronucleus is located at the side of the aster, female pronuclear transport will generate pulling forces along the side portion of the sperm aster, which indeed causes minor lateral movements of the sperm aster toward the female pronucleus as it is being transported toward the male pronucleus (Chambers, 1939; Tanimoto et al., 2016). Furthermore, retrograde transport of the female pronucleus along the front of the sperm aster does not increase sperm aster migration rates (Tanimoto et al., 2016), as would be expected in a MT-length-dependent cytoplasmic pulling model, which we hypothesize is likely because the sperm aster is anchored to the rear cortex (Figure 3), and migration rates are primarily determined by growth rates of the rear portion of the sperm aster (Figure 2). Together, these data highlight that although retrograde cytoplasmic transport of the female pronucleus is dynein dependent and does generate pulling force along the sperm aster, it is not the predominant force driving aster centration and is not essential to successfully center the sperm aster in sea urchins.

Third, work done by Tanimoto et al. (2016) using laser ablation of the side of the aster as a read out for pushing versus pulling during migration concluded that aster migration away from the side of ablation indicated pulling forces. Importantly, a role for dynein in these movements away from the side of ablation was not tested. A more direct way to determine if the aster is pushed or pulled to the center is the experiment proposed by Reinsch and Gonczy (1998), hypothesizing that ablation of the rear portion of the aster will halt migration in a MT pushing model. When we ablated the rear portion of the sperm aster, migration came to a halt (Figures 5A–5C; Video S6). We instead favor the idea that any dynein-dependent pulling on side portions of the aster may maintain directionality of aster movement (Tanimoto et al., 2018) as it is being pushed to the zygote center by polymerization of rear MTs against the cortex. Consistent with this idea, we found that p150-CC1-mediated inhibition of dynein results in occasional rotation of the sperm aster as it approaches the center (Video S5), suggesting that dynein inhibition causes defects in the direction of aster migration. This "steering" role for lateral astral MTs is also supported by ablations of side portions of the aster, which results in directional defects during aster migration (Tanimoto et al., 2016). We hypothesize that this phenotype could be due to a lack of dynein-dependent force balancing along the sides of the aster when dynein is inhibited or by a lack of dynein/dynactin anchoring of astral MTs at the cell cortex.

A final inconsistency we found between our data and the MT-length-dependent cytoplasmic pulling model was in our aster MT density measurements. We found greater MT density in the rear portion of the sperm aster than in the front, which was considered in the 1D MT-length-dependent pulling model (Tanimoto et al., 2016; Figures 1E, S1D, and S1E). In a cytoplasmic pulling model, a greater number of MTs in the aster rear should also allow more dynein-dependent force generation on the rear relative to the front, which is not the case because asters would then move toward the rear cortex rather than toward the cell center. Instead, the increased density we observed in the rear portions of the aster may be consistent with MT branching and/or bundling, allowing for MT-based pushing. A wealth of recent *in vitro* studies indicated that acentrosomal nucleation of MTs leads to large asters formed from branched MTs networks in *Xenopus* extracts (Alfaro-Aco et al., 2017; Petry et al., 2013; Song et al., 2018; Thawani et al., 2019). Additionally, MT branching *in vivo* was recently discovered to occur in mitotic asters of *Drosophila* S2 cells (Verma and Maresca, 2019). Furthermore,

through a similar mechanism used for nucleating branching, MT bundle formation was recently shown to play a role in guiding spindle MTs to kinetochores (David et al., 2019). We hypothesize that MT branching/bundling could permit a pushing mechanism based on the growth of numerous short MTs polymerizing against the cortex during large aster positioning, which would prevent MT buckling and slipping. Similarly, bundling of MTs should increase the amount of compression force allowed on MTs before buckling occurs. Interestingly, EB1-GFP comets along rear MTs in the aster appear to traverse over the same MT track multiple times, which partially accounts for the greater MT density along rear portions of the aster (Figures 1E, S1D, and S1E; Video S1). This "waterfall" pattern of the EB1-GFP signal we observed is similar to the multiple EB3-GFP comets detected along MT tracks in bundled spindle MTs (David et al., 2019), suggesting that bundling may also occur in MTs within the rear portion of the sperm aster. Finally, it is worth noting that studies at first cleavage division in other invertebrates in which one mitotic aster is much larger than the sister aster suggested that as the large aster grows, it pushes the whole mitotic apparatus toward the opposite pole, resulting in unequal cell division (Ren and Weisblat, 2006). Consequently, pushing forces generated by astral growth may be used during mitosis as well. Future work investigating potential MT bundling/branch factors within the sea urchin sperm aster may provide more details for how a large aster can be pushed through the viscous cytoplasm.

Our study also revealed that the sperm aster was robustly anchored to the rear cortex in the sea urchin zygote (Figure 3; Video S3), which is similar to the anchoring of meiotic maternal centrioles in other systems (Fabritius et al., 2011). We found that membrane invaginations, likely where the sperm aster is anchored to the rear cortex, were only observed when the sperm aster captured the female pronucleus, indicating that pulling forces are negligible until the male and female pronuclei engage (Figures 3D and 3E; Video S3). Furthermore, in fertilized enucleated zygotes, we found that the sperm aster still migrated to the cell center in the absence of engagement between the male and female pronuclei (Video S3). These data suggest that force production from retrograde transport of the female pronucleus is not essential for sperm aster centration. An important question moving forward is how and why the sperm aster is anchored to the cortex. We predict, based on our results, that dynein is required to anchor the aster to the cortex as in other systems (Fujita et al., 2015; Kotak et al., 2012). Here, we hypothesized that attachment of the aster to the rear cortex by dynein/dynactin, in combination with branching/bundling, helps prevent slipping of MTs as they polymerize and push the aster to the zygote center. Indeed, previous work suggests that pushing is more effective when slipping is reduced and that puling is more effective when slipping is increased (Pavin et al., 2012). Additionally, dynein may be required to regulate MT growth and anchoring at the cortex (Laan et al., 2012). Consistent with this idea, the rotational phenotype of asters in p150-CC1 injected cells could be due to an overgrowth of unanchored MTs once the aster is centered or near the centered, causing MT buckling. Thus, our study provides an *in vivo* framework for future studies to elucidate the physical nature of polymerization-induced pushing forces at the cell cortex during large aster positioning.

STAR★METHODS

Detailed methods are provided in the online version of this paper and include the following:

- KEY RESOURCES TABLE
- RESOURCE AVAILABILITY
  - Lead Contact
  - Materials Availability
  - Data and Code Availability
- EXPERIMENTAL MODEL AND SUBJECT DETAILS
  - Lytechinus Pictus
- METHOD DETAILS
  - Microscopy
  - Cellular orientation used to define front and rear portions of the aster
  - Live MT and MT plus-end imaging
  - Fixed MT imaging
  - Live pronuclei imaging
  - Processing and analysis of confocal microscopy images
  - Immunostaining
  - Cortical isolations
  - Microinjections
  - Pharmacological inhibitors
  - Egg nuclear sedimentation and enucleation
  - Chemical ablations
- QUANTIFICATION AND STATISTICAL ANALYSIS

SUPPLEMENTAL INFORMATION

Supplemental Information can be found online at https://doi.org/10.1016/j.celrep.2020.108213.

ACKNOWLEDGMENTS

We would like to thank Dr. Jesse Gatlin for sending us the Tau-mCherry fusion protein for imaging live MTs. We would also like to thank Dr. Timothy Mitchison, Dr. Christine Field, and Dr. James Pelletier for supplying us with CA4, p150-CC1, and EB1-GFP peptides, as well as for fruitful discussions. Finally, we would like to thank Dr. Charles Shuster and Leslie Toledo-Jacobo for constructive feedback when preparing the manuscript. We thank Bret Judson and the Boston College Imaging Core for infrastructure and support. This material is based upon work supported by NSF grant no. 124425 to D.R.B.

AUTHOR CONTRIBUTIONS

J.L.M. conceived and designed experiments, performed the experiments, analyzed and interpreted the results, and wrote the manuscript. S.N.d.M. helped obtain and image enucleated eggs. D.R.B. conceived the project, designed experiments, and co-wrote and provided input and feedback for the manuscript.

DECLARATION OF INTERESTS

The authors declare no competing interests.

Received: March 6, 2019
Revised: January 12, 2020
Accepted: September 10, 2020
Published: October 6, 2020

REFERENCES

Alfaro-Aco, R., Thawani, A., and Petry, S. (2017). Structural analysis of the role of TPX2 in branching microtubule nucleation. J. Cell Biol. *216*, 983–997.

Barbosa, D.J., Duro, J., Prevo, B., Cheerambathur, D.K., Carvalho, A.X., and Gassmann, R. (2017). Dynactin binding to tyrosinated microtubules promotes centrosome centration in C. elegans by enhancing dynein-mediated organelle transport. PLoS Genet. *13*, e1006941.

Bergen, L.G., Kuriyama, R., and Borisy, G.G. (1980). Polarity of microtubules nucleated by centrosomes and chromosomes of Chinese hamster ovary cells in vitro. J. Cell Biol. *84*, 151–159.

Bestor, T.H., and Schatten, G. (1981). Anti-tubulin immunofluorescence microscopy of microtubules present during the pronuclear movement of sea urchin fertilization. Dev. Biol. *88*, 80–91.

Bjerknes, M. (1986). Physical theory of the orientation of astral mitotic spindles. Science *234*, 1413–1416.

Burgess, D.R., and Schroeder, T.E. (1977). Polarized bundles of actin filaments within microvilli of fertilized sea urchin eggs. J. Cell Biol. *74*, 1032–1037.

Chambers, E.L. (1939). The Movement of the Egg Nucleus in Relation to the Sperm Aster in the Echinoderm Egg. J. Exp. Biol. *16*, 409–424.

Costache, V., Hebras, C., Pruliere, G., Besnardeau, L., Failla, M., Copley, R.R., Burgess, D., Chenevert, J., and McDougall, A. (2017). Kif2 localizes to a subdomain of cortical endoplasmic reticulum that drives asymmetric spindle position. Nat. Commun. *8*, 917.

Culley, S., Albrecht, D., Jacobs, C., Pereira, P.M., Leterrier, C., Mercer, J., and Henriques, R. (2018). Quantitative mapping and minimization of super-resolution optical imaging artifacts. Nat. Methods *15*, 263–266.

David, A.F., Roudot, P., Legant, W.R., Betzig, E., Danuser, G., and Gerlich, D.W. (2019). Augmin accumulation on long-lived microtubules drives amplification and kinetochore-directed growth. J. Cell Biol. *218*, 2150–2168.

De Simone, A., Spahr, A., Busso, C., and Gönczy, P. (2018). Uncovering the balance of forces driving microtubule aster migration in C. elegans zygotes. Nat. Commun. *9*, 938.

Dogterom, M., and Yurke, B. (1997). Measurement of the Force-Velocity Relation for Growing Microtubules. Science *278*, 856–860.

Dogterom, M., Kerssemakers, J.W., Romet-Lemonne, G., and Janson, M.E. (2005). Force generation by dynamic microtubules. Curr. Opin. Cell Biol. *17*, 67–74.

Fabritius, A.S., Ellefson, M.L., and McNally, F.J. (2011). Nuclear and spindle positioning during oocyte meiosis. Curr. Opin. Cell Biol. *23*, 78–84.

Firestone, A.J., Weinger, J.S., Maldonado, M., Barlan, K., Langston, L.D., O'Donnell, M., Gelfand, V.I., Kapoor, T.M., and Chen, J.K. (2012). Small-molecule inhibitors of the AAA+ ATPase motor cytoplasmic dynein. Nature *484*, 125–129.

Fujita, I., Yamashita, A., and Yamamoto, M. (2015). Dynactin and Num1 cooperate to establish the cortical anchoring of cytoplasmic dynein in S. pombe. J. Cell Sci. *128*, 1555–1567.

Gönczy, P., Pichler, S., Kirkham, M., and Hyman, A.A. (1999). Cytoplasmic Dynein Is Required for Distinct Aspects of Mtoc Positioning, Including Centrosome Separation, in the One Cell Stage Caenorhabditis elegans Embryo. J. Cell Biol. *147*, 135–150.

Goshima, G., Nédélec, F., and Vale, R.D. (2005). Mechanisms for focusing mitotic spindle poles by minus end–directed motor proteins. J. Cell Biol. *171*, 229–240.

Hamaguchi, M.S., and Hiramoto, Y. (1986). Analysis of the Role of Astral Rays in Pronuclear Migration in Sand Dollar Eggs by the Colcemid-UV Method. Dev. Growth Differ. *28*, 143–156.

Harris, P., Osborn, M., and Weber, K. (1980). Distribution of tubulin-containing structures in the egg of the sea urchin Strongylocentrotus purpuratus from fertilization through first cleavage. J. Cell Biol. *84*, 668–679.

Harvey, E.B. (1933). Development of the Parts of Sea Urchin Eggs Separated by Centrifugal Force. Biol. Bull. *64*, 125–148.

Henson, J.H., Samasa, B., and Burg, E.C. (2019). High resolution imaging of the cortex isolated from sea urchin eggs and embryos. Methods Cell Biol. *151*, 419–432.

Holy, T.E., Dogterom, M., Yurke, B., and Leibler, S. (1997). Assembly and positioning of microtubule asters in microfabricated chambers. Proc. Natl. Acad. Sci. *94*, 6228–6231.

Ishihara, K., Nguyen, P.A., Groen, A.C., Field, C.M., and Mitchison, T.J. (2014). Microtubule nucleation remote from centrosomes may explain how asters span large cells. Proc. Natl. Acad. Sci. *111*, 17715–17722.

Ishihara, K., Korolev, K.S., and Mitchison, T.J. (2016). Physical basis of large microtubule aster growth. eLife *5*, e19145.

Kimura, K., and Kimura, A. (2011). Intracellular organelles mediate cytoplasmic pulling force for centrosome centration in the Caenorhabditis elegans early embryo. Proc. Natl. Acad. Sci. *108*, 137–142.

Kimura, A., and Onami, S. (2005). Computer simulations and image processing reveal length-dependent pulling force as the primary mechanism for C. elegans male pronuclear migration. Dev. Cell *8*, 765–775.

Kotak, S., Busso, C., and Gönczy, P. (2012). Cortical dynein is critical for proper spindle positioning in human cells. J. Cell Biol. *199*, 97–110.

Kozlowski, C., Srayko, M., and Nedelec, F. (2007). Cortical microtubule contacts position the spindle in C. elegans embryos. Cell *129*, 499–510.

Laan, L., Pavin, N., Husson, J., Romet-Lemonne, G., van Duijn, M., López, M.P., Vale, R.D., Jülicher, F., Reck-Peterson, S.L., and Dogterom, M. (2012). Cortical dynein controls microtubule dynamics to generate pulling forces that position microtubule asters. Cell *148*, 502–514.

Longo, F.J., and Anderson, E. (1968). The fine structure of pronuclear development and fusion in the sea urchin, Arbacia punctulata. J. Cell Biol. *39*, 339–368.

Merdes, A., Heald, R., Samejima, K., Earnshaw, W.C., and Cleveland, D.W. (2000). Formation of Spindle Poles by Dynein/Dynactin-Dependent Transport of Numa. J. Cell Biol. *149*, 851–862.

Minc, N., Burgess, D., and Chang, F. (2011). Influence of cell geometry on division-plane positioning. Cell *144*, 414–426.

Mooney, P., Sulerud, T., Pelletier, J.F., Dilsaver, M.R., Tomschik, M., Geisler, C., and Gatlin, J.C. (2017). Tau-based fluorescent protein fusions to visualize microtubules. Cytoskeleton (Hoboken) *74*, 221–232.

Murata, T., Sonobe, S., Baskin, T.I., Hyodo, S., Hasezawa, S., Nagata, T., Horio, T., and Hasebe, M. (2005). Microtubule-dependent microtubule nucleation based on recruitment of γ-tubulin in higher plants. Nat. Cell Biol. *7*, 961–968.

Negishi, T., Miyazaki, N., Murata, K., Yasuo, H., and Ueno, N. (2016). Physical association between a novel plasma-membrane structure and centrosome orients cell division. eLife *5*, e16550.

Nguyen-Ngoc, T., Afshar, K., and Gönczy, P. (2007). Coupling of cortical dynein and G α proteins mediates spindle positioning in Caenorhabditis elegans. Nat. Cell Biol. *9*, 1294–1302.

Paix, A., Le Nguyen, P.N., and Sardet, C. (2011). Bi-polarized translation of ascidian maternal mRNA determinant pem-1 associated with regulators of the translation machinery on cortical Endoplasmic Reticulum (cER). Dev. Biol. *357*, 211–226.

Pavin, N., Laan, L., Ma, R., Dogterom, M., and Jülicher, F. (2012). Positioning of microtubule organizing centers by cortical pushing and pulling forces. New J. Phys. *14*, 105025.

Payne, C., Rawe, V., Ramalho-Santos, J., Simerly, C., and Schatten, G. (2003). Preferentially localized dynein and perinuclear dynactin associate with nuclear pore complex proteins to mediate genomic union during mammalian fertilization. J. Cell Sci. *116*, 4727–4738.

Peng, C.J., and Wikramanayake, A.H. (2013). Differential regulation of dishevveled in a novel vegetal cortical domain in sea urchin eggs and embryos: implications for the localized activation of canonical Wnt signaling. PLoS One *8*, e80693.

Petry, S., Groen, A.C., Ishihara, K., Mitchison, T.J., and Vale, R.D. (2013). Branching microtubule nucleation in Xenopus egg extracts mediated by augmin and TPX2. Cell *152*, 768–777.

Pollard, T.D., and O'Shaughnessy, B. (2019). Molecular Mechanism of Cytokinesis. Annu. Rev. Biochem. *88*, 661–689.

Quintyne, N.J., Gill, S.R., Eckley, D.M., Crego, C.L., Compton, D.A., and Schroer, T.A. (1999). Dynactin is required for microtubule anchoring at centrosomes. J. Cell Biol. *147*, 321–334.

Rappaport, R. (1961). Experiments concerning the cleavage stimulus in sand dollar eggs. J. Exp. Zool. *148*, 81–89.

Rappaport, R., and Rappaport, B.N. (1984). Division of constricted and urethane-treated sand dollar eggs: a test of the polar stimulation hypothesis. J. Exp. Zool. *231*, 81–92.

Redemann, S., Pecreaux, J., Goehring, N.W., Khairy, K., Stelzer, E.H.K., Hyman, A.A., and Howard, J. (2010). Membrane invaginations reveal cortical sites that pull on mitotic spindles in one-cell C. elegans embryos. PLoS One *5*, e12301.

Reinsch, S., and Gonczy, P. (1998). Mechanisms of nuclear positioning. J. Cell Sci. *111*, 2283–2295.

Reinsch, S., and Karsenti, E. (1997). Movement of nuclei along microtubules in Xenopus egg extracts. Curr. Biol. *7*, 211–214.

Ren, X., and Weisblat, D.A. (2006). Asymmetrization of first cleavage by transient disassembly of one spindle pole aster in the leech Helobdella robusta. Dev. Biol. *292*, 103–115.

Roegiers, F., Djediat, C., Dumollard, R., Rouviere, C., and Sardet, C. (1999). Phases of cytoplasmic and cortical reorganizations of the ascidian zygote between fertilization and first division. Development *126*, 3101–3117.

Roossien, D.H., Miller, K.E., and Gallo, G. (2015). Ciliobrevins as tools for studying dynein motor function. Front. Cell. Neurosci. *9*, 252.

Saito, T.T., Okuzaki, D., and Nojima, H. (2006). Mcp5, a meiotic cell cortex protein, is required for nuclear movement mediated by dynein and microtubules in fission yeast. J. Cell Biol. *173*, 27–33.

Sallé, J., Xie, J., Ershov, D., Lacassin, M., Dmitrieff, S., and Minc, N. (2018). Asymmetric division through a reduction of microtubule centering forces. J. Cell Biol. *218*, 771–782.

Schatten, G. (1981). Sperm incorporation, the pronuclear migrations, and their relation to the establishment of the first embryonic axis: time-lapse video microscopy of the movements during fertilization of the sea urchin Lytechinus variegatus. Dev. Biol. *86*, 426–437.

Song, J.-G., King, M.R., Zhang, R., Kadzik, R.S., Thawani, A., and Petry, S. (2018). Mechanism of how augmin directly targets the γ-tubulin ring complex to microtubules. J. Cell Biol. *217*, 2417–2428.

Strickland, L.I., Donnelly, E.J., and Burgess, D.R. (2005). Induction of cytokinesis is independent of precisely regulated microtubule dynamics. Mol. Biol. Cell *16*, 4485–4494.

Tanimoto, H., and Minc, N. (2017). Quantitative approaches for the study of microtubule aster motion in large eggs. Methods Cell Biol. *139*, 69–80.

Tanimoto, H., Kimura, A., and Minc, N. (2016). Shape–motion relationships of centering microtubule asters. J. Cell Biol. *212*, 777–787.

Tanimoto, H., Sallé, J., Dodin, L., and Minc, N. (2018). Physical forces determining the persistency and centering precision of microtubule asters. Nat. Phys. *14*, 848–854.

Thawani, A., Stone, H.A., Shaevitz, J.W., and Petry, S. (2019). Spatiotemporal organization of branched microtubule networks. eLife *8*, e43890.

Tran, P.T., Marsh, L., Doye, V., Inoué, S., and Chang, F. (2001). A Mechanism for Nuclear Positioning in Fission Yeast Based on Microtubule Pushing. J. Cell Biol. *153*, 397–412.

Verma, V., and Maresca, T.J. (2019). Direct observation of branching MT nucleation in living animal cells. J. Cell Biol. *218*, 2829–2840.

Wühr, M., Tan, E.S., Parker, S.K., Detrich, H.W., 3rd, and Mitchison, T.J. (2010). A model for cleavage plane determination in early amphibian and fish embryos. Curr. Biol. *20*, 2040–2045.

Yi, J., Wu, X., Chung, A.H., Chen, J.K., Kapoor, T.M., and Hammer, J.A. (2013). Centrosome repositioning in T cells is biphasic and driven by microtubule end-on capture-shrinkage. J. Cell Biol. *202*, 779–792.

STAR★METHODS

KEY RESOURCES TABLE

REAGENT or RESOURCE	SOURCE	IDENTIFIER
Antibodies		
Anti-α-Tubulin, clone DM1A, Alexa Fluor 488 conjugate (Mouse monoclonal)	MilliporeSigma	Cat# 16-232; RRID: AB_441973
Chemicals, Peptides, and Recombinant Proteins		
Protamine sulfate	Sigma-Aldrich	P4020
Urethane, Minimum 99%	Sigma-Aldrich	U2500
Hexylene glycol 99%	Sigma-Aldrich	112100
Hoescht Solution	ThermoFisher Scientifi	33342
Caged-Combretastatin 4A	Gift from Timothy Mitchison, Christine Field, and James Pelletier, Harvard University, (Wühr et al., 2010)	N/A
Tau peptide-mCherry	Gift from Jessie Gatlin, University of Wyoming (Mooney et al., 2017)	N/A
P150-CC1 peptide fragment	Gift from Timothy Mitchison, Christine Field, and James Pelletier, Harvard University, (Wühr et al., 2010)	N/A
EB1 peptide-GFP	Gift from Timothy Mitchoson, Christine Field, and James Pelletier, Harvard University	N/A
VALAP	Vaseline, Lanolin, Paraffin in 1:1:1 mass ratio	N/A
Ciliobrevin D	Sigma-Aldrich	250401
Experimental Models: Organisms/Strains		
Sea Urchin *Lytechinus Pictus*	Marinus Scientific, LLC.	http://www.marinusscientific.com/
Software and Algorithms		
ImageJ	NIH	https://imagej.nih.gov/ij/index.html
Zen Black	Carl Zeiss Microscopy, LLC	https://www.zeiss.com/microscopy/us/downloads.html
Zen Blue	Carl Zeiss Microscopy, LLC	https://www.zeiss.com/microscopy/us/downloads.html
LAS AF	Leica Microsystems	https://www.leica-microsystems.com/products/microscope-software/p/leica-las-x-ls/
Graphpad Prism 8.2.1 for Windows 10	(Culley et al., 2018) Graphpad Software, La Jolla California USA	https://www.graphpad.com

RESOURCE AVAILABILITY

Lead Contact

Further information and requests for resources and reagents should be directed to and will be fulfilled by the Lead Contact, David Burgess (david.burgess@bc.edu).

Materials Availability

This study did not generate new unique reagents.

Data and Code Availability

This study did not generate new code. The published article contains all datasets generated in this study.

EXPERIMENTAL MODEL AND SUBJECT DETAILS

Lytechinus Pictus

Sea urchins *Lytechinus pictus* were purchased from Marinus Scientific (Long Beach, Ca). Animals were maintained in a temperature-controlled aquarium at 16C filled with artificial sea water (ASW) made from Instant Ocean mix (30-35 ppm). Urchins were exposed to light cycles of 12 hour intervals. Gametes were collected the day of use by intracoelomic injection of 0.5M KCl. Adult L. pictus have no sexual dimorphism, so sex could only be determined after spawning. Sperm could be stored and used for up to ~5 days post-collection. Sperm was diluted and activated in filtered sea water from the Woods Hole Marine Biological Laboratories (MBLSW) at a 1:1000 dilution. Eggs were collected directly into MBLSW. For fixed imaging, eggs were fertilized and passed through a Nitex membrane (86-102 um) several times to remove fertilization envelopes and raised in filtered sea water at the appropriate temperatures until our time points of interest. For live imaging, jelly coats were removed from eggs by several passes through a 102 um Nitex membrane.

METHOD DETAILS

Microscopy

Live and fixed-cell imaging of MTs and MT plus-ends was performed on a Zeiss 880 laser point scanning confocal microscope mounted with an Airyscan detector using a 40x 1.1 NA water immersion objective. Samples were maintained on a water-cooled stage at 16C connected to a refrigerated water circulator. Fixed MTs were imaged using an Argon laser, while live MTs were imaged using a 488 or 561 nm laser, depending on the fluorophore. Airyscan post acquisition processing was performed using Zen Blue software. Live-cell imaging of the male pronucleus was performed using a Leica SP5 laser point scanning confocal microscope with a 40x 1.1 NA water immersion objective and a 405 nm UV laser. The room for this microscope was maintained at 14-16 C.

Cellular orientation used to define front and rear portions of the aster

In all image acquisition throughout this study, cells were selected for in which the sperm enters ± 10 um from the cell equator along the Z axis (see Figure S1A). This equatorial fertilization ensures that the aster migrates along the cell equator without any deviations along the Z axis. In this way, any portions of the aster that are slanted in the Z axis are defined as "top" or "bottom," while all portions of the aster parallel to the migration axis and coverslip are defined as "front' or "rear" (Figure S1A). This orientation helps to exclude any top and bottom portions of the aster from our analysis of aster geometry. In live-cell imaging slanted portions of the aster leave the single z-slice imaging plane, effectively excluding them from analysis. Similarly, in our immunofluorescence analysis, due to the spherical nature of the aster, slanted portions of the sperm aster do not extend to the maximum front and rear boundaries of the sperm aster in the X/y axis (Figure S1A). Because we measure from the MTOC to the maximum aster boundaries in front and rear portions, as outlined below, these slanted top and bottom portions of the aster are excluded from our quantifications (Figure S1A).

Live MT and MT plus-end imaging

Tau-mCherry and EB1-GFP-labeled MT plus-ends and MTs were imaged on a Zeiss 880 Airyscan with a 40x 1.1 NA water immersion objective. Movies for Figure 2 were imaged at 5, 10, and 15 minute time points post sperm addition. Movies for Figure 1 were acquired at different time points based on how far the aster moved from the site of sperm entry, determined by EB1-GFP detection of the MTOC. In order to thoroughly sample the MTs and their plus-ends throughout migration, these time points were standardized to 10, 15, 20, 25, 30, and 35 μm of distance moved from the site of sperm entry (Figures 1A and 1B; Video S1). For both figures, single z-slices of EB1-GFP through the middle of the centrosome were acquired at 2.5 s intervals for at least 30 s at each time point, followed by a single z-slice of Tau-mCherry signal. For Figures 4 and 5, single z-slices (10-15 s/frame) of Tau-mCherry were acquired at the centrosome throughout the duration of aster migration.

Fixed MT imaging

To image DM1A-labeled α-tubulin in whole zygotes, fixed immunofluorescence imaging was performed on a laser point scanning confocal microscope (Zeiss 880 Airyscan), controlled by Zen Black software with a 40x 1.1 NA water immersion objective. 3D volumes (40 μm, composed of 20 z sections at 2 μm intervals) were acquired for each sample to ensure the entire aster (Figures 1C, 3D, and 4A) was acquired in each dataset. Only zyogtes in which the centrosomes were ± 10 μm from the cell equator were imaged in order to ensure front and rear portions of the aster could be defined (see processing and analysis below for definitions). Isolated cortices were imaged on a Zeiss LSM 780 (Marine Biology Laboratories, Woodshole, MA), controlled by Zen Black with a 40X 1.2 NA water immersion objective. 3D volumes (10 μm, composed of 10 μm sections at 1 μm intervals, or roughly the thickness of the cortex) were acquired (Figure 3A).

Live pronuclei imaging

Eggs and sperm were incubated with Hoescht at a final concentration of 1 ug/ml to allow staining of male and female pronuclei. Eggs were then added to glass bottom dishes (35 × 10 mm) and allowed to settle to minimize movement during imaging. Hoescht-labeled pronuclei (movies for Figures S2B and 3C; Video S3) were imaged using a Leica SP5 LSM, controlled by LAS AF software, with a 40x 1.1 NA water immersion objective and a 405 nm UV laser. Zygotes in which the sperm entered ± 10 μm from the cell equator were

chosen for imaging to reduce the 3D volume required to capture the entire pronuclear migration process. 3D volumes of 40 μm at 2 μm intervals were acquired every 10-15 s from sperm penetration until male pronuclear centration was complete.

Processing and analysis of confocal microscopy images

Measuring aster Lfront and Lrear with EB1-GFP signal

The exact distance of individual EB1-GFP comets from the centrosome could not be reliably measured because the density of comets was too high, especially in rear portions of the aster. We therefor converted EB1-GFP movies (Figures 1A, 1B, 2D, and 2E; Videos S1 and S2) to maximum intensity temporal projections, which plots comet movement over time in a single 2D image. These plots revealed smooth MT tracks, which represent individual MTs and/or MT bundles within the sperm asters. We then measured the distance from the most distal portion of EB1-tracks to the MTOC using FIJI (imageJ). We defined the front portions of the aster as an ROI extending in front of the MTOC (cytoplasmic facing) at 45 degree angles relative to the directional axis of aster migration, which in total produces a 90 degree ROI. Likewise, the rear portion of the aster was defined as an ROI extending behind the MTOC, between the MTOC and the cortical face containing the site of sperm entry, at 45 degree angles on each side of the directional axis of aster migration. These definitions thus excluded MTs on the remaining 90 degree ROIs on each side portion of the aster. All EB1-GFP tracks in each front and rear ROI at each of our time points were then averaged for each zygote to define the Lfront and Lrear, respectively. We then calculated a cumulative average of the Lfront and Lrears of all of the zygotes to obtain an average Lfront and Lrear, or front and rear radii. Differences between average LFront and Lrear were then tested for statistical significance ($p < 0.05$) using a 2 way ANOVA followed by a Tukey's multiple comparisons test using Graphpad Prism 8. In Figure 2E average Lfront and Lrear were also compared to distance moved (see below for aster migration rate quantification methods). In these quantifications, differences between Lfront or Lrear portions of the aster and distance moved were also individually tested for statistical significance ($p < 0.05$) by also using a 2-way ANOVA followed by Tukey's multiple comparisons.

Measuring aster Lfront and Lrear with Tau-mCherry signal and DM1A α-tubulin

Following EB1-GFP time-lapse acquisition, we obtained 1 frame of a single z-slice of Tau-mCherry signal from the same zygote, which allowed us the advantage of measuring lengths of potentially stable, non-growing MTs. We applied the same ROIs used to define front and rear portions of the aster during our EB1-GFP MT length measurements, and measured the lengths of the most distal tip of all detectable MTs/bundles to the centrosome in front and rear ROIs. We then averaged the lengths MT/bundles in front and rear ROIs to define Lfront and Lrear for each cell, and further cacluated the averages of Lfront and Lrear from all zygotes, similar to our EB1-GFP MT length measurements. Differences between average Lfront and Lrear from all zygotes were then tested for statistical significance ($p < 0.05$) using a 2-way ANOVA followed by Tukey's multiple comparisons. We applied the same quantifications to maximum intensity projections of asters obtained from our 3D volumes of fixed immunofluorescence of DM1A-tagged α-tubulin (Figures 1C and 1D).

Quantifying EB1-GFP and Tau-mCherry Fluorescence intensity

To estimate MT density in front and rear portions we converted each of our EB1-GFP time-lapse videos from Figure 1 into average temporal projections using Fiji (ImageJ). We then applied the same defined front and rear ROIs used in our MT/bundle length measurements. We manually measured fluorescence intensities as a function of distance from the centrosome in each ROI by using manually drawn lines in Fiji (ImageJ), perpendicular to the directional axis of aster migration at 2 μm intervals from the centrosome. The EB1-GFP background signal (and non-astral MTs) was estimated by measuring the average fluorescence intensity of three 10 μm diameter circles randomly placed in cytoplasm that is void of astral MTs. We then subtracted the average background signal from our fluorescence intensity measurements made in the aster. Next, we normalized our front and rear astral fluorescence intensities to the average fluorescence intensities of the MTOC, measured in a 2 μm diameter circle manually placed around the MTOC. This provided us with normalized average intensities of EB1-GFP signal at 2 μm intervals from the centrosome in front and rear portions of the sperm aster. We then calculated the statistical differences ($p < 0.05$) between intensity profiles from front and rear portions of the aster using a 2-way ANOVA followed by Sidak's multiple comparisons test in Graphpad Prism 8. We applied the same method to our single z-slice/single time frame images of Tau-mCherry signal obtained after EB1-GFP time lapse videos from the same cells, which yields similar intensity profiles in rear and front portions of the aster (Figure S1C).

Tracking aster migration rates using EB1-GFP signal and Hoescht-labeled male and female pronuclei

Confocal time-lapse videos of hoescht-labeled pronuclei (Figures S2B and 3C; Video S3) were converted to maximum intensity projections of the 3D volumes. We then tracked how far each pronucleus moved at each 10-15 s time interval by hand using Fiji (ImageJ). Because only zygotes in which sperm entry was at ± 10 μm from the cell equator, deviations in Z were rare, similar to what was seen by Tanimoto et al. (2016). The average distance moved for each time point was then calculated and plotted as distances versus time curves.

Aster migration rates were also quantified from confocal time-lapse videos of single z-slice EB1-GFP labeled MTOCs by measuring the distance between the MTOC and the site of sperm entry at 5, 10, and 15-minute time points post-fertilization using Fiji (ImageJ). These rates were then averaged and compared with the average rates obtained from Hoescht-labeled pronuclear tracking quantifications using Graphpad Prism 8, which produced no significant difference ($p < 0.05$) in a 2-way ANOVA followed by Tukey's multiple comparison.

The three separate phases of aster migration (Figure S2B) where determined by three regions of differential migration rates on distance versus time plots: 0-5 min post fertilization,5-10 minutes post fertilization, and 10-15 minutes post fertilization. Aster speed

during each of these three phases was determined by linear fitting of each phase, which yielded the slope of the curve throughout each phase of migration (2.29 ± 0.09 μm, 4.8 ± 2 μm, and 1.250 ± 0.25 μm for phase 1, 2, and 3 respectively). The slopes were determined to be statistically different ($p < 0.001$) by performing an ANCOVA analysis of the three curves. All statistical analysis for this method were performed in Graphpad Prism 8.

Comparison of Lfront/Lrear and migration rates

Lfront and Lrear, quantified from our EB1-GFP length measurements in untreated zygotes were determined over 5, 10, and 15 minute time points and compared to our migration rate data (Figure S2C). We determined if there are any changes in Lfront and Lrear associated with the changes in migration rates by fitting the computed aster migration and Lfront/Lrear curves to a logistic model, which predicts an increased growth/migration rates (initial phase of aster migration) to a constant maximum growth/migration rate (second phase of migration), followed by a decrease in growth/migration rates as MTs reach their maximum lengths. Analysis was performed using Graphpad Prism 8.

Tracking aster migration distance using Tau-mCherry signal

To study the movement of Tau-mCherry labeled sperm asters, we measured the distance of the centrosome to the site of sperm entry manually using Fiji (ImageJ) at each 10-15 s intervals in our single z-plane videos (Videos S5, S6, and S7). We then calculated the total average distance moved among all of our samples for each time point. The average distance was then plotted either as a function of time post sperm entry (Figure 4D), or as a function of time before and after UV-activation of CA4 (Figure 5C). Statistical differences in average distance moved at each ($p < 0.05$) between conditions were calculated using a 2-way ANOVA followed by Sidak's multiple comparisons test (Figures 4D and 5C).

Quantification of equatorial division

Eggs were fertilized in the presence of 50 nM CA4 or DMSO (control), protected from light, and incubated to the two-cell stage. They were then imaged under a brightfield dissecting microscope. Only embryos positioned with their long axis perpendicular to the bottom of the dish were chosen for analysis in order to accurately measure diameter of each of the two cells within each embryo. Diameter was measured from the plasma membrane between the two cells to the cell pole for each cell. The slightly smaller of the two cells was then divided by the slightly larger of the two cells to obtain the cell:cell ratio (Figure 5E). This experiment was repeated on 3 different batches of eggs from 3 separate female urchins.

Measuring the distance of the male pronucleus from the cell center

The center of the cell was defined as one half the cell diameter (or radius) as measured from the plasma membrane to the cell interior in maximum intensity projections of time-lapse confocal images. The distance from the center of the male pronucleus at the end of migration was then measured to this defined cell center using Fiji (ImageJ). The average distance was then calculated for all of our samples in each condition. Differences in averages were then calculated using a standard ANOVA in Graphpad Prism 8.

Immunostaining

Whole-cell zygotes were fixed and permeabilized in bulk (1.5 mL Eppendorf tubes) at the indicated time points (Figures 1C and 4A) using a fixation buffer composed of 100 mM HEPES (pH 7.0), 50 mM EGTA (pH 7.0), 10 mM MgSO4, 400 mM dextrose, 2% formaldehyde, and 0.2% Triton-X. Samples were incubated for 1 hr at room temperature with gentle agitation, rinsed 3X with (PBST) and left to sit overnight in PBST. We blocked samples in 5% BSA/PBST for 2 hr at room temperature on a rocker. Samples were then transferred to Alexa 488 conjugated DM1A alpha tubulin antibody (1:1000) (EMD Millipore) in 5% BSA/PBST for 48 hr at room temperature on a rocker. We rinsed the samples 3X in PBST over the course of 2 hours. Samples were mounted in 90% glycerol on chamber slides made from double-sided tape using 24 × 24 mm coverslips with a thickness no. 1.5 and sealed with VALAP.

Cortical isolations

Zygote cortical isolation procedures were adapted from Burgess and Schroeder (1977). Eggs were dejellied by incubation in acidic sea water (pH 4.0) for 3 min before transferring them back to filtered sea water. We then induced polyspermy by fertilizing the eggs in sea water containing 4 mg/ml of soy bean trypsin inhibitor (SBTI). At 5 minutes post-sperm addition zygote were settled onto protamine sulfate-coated coverslips. 3-5 minutes later (8 to 10 minutes post-sperm addition), zygotes were sheared by pipetting an isotonic buffer containing 0.8 M mannitol, 5mM MgCl2, 10 mM EGTA, and 10 mM HEPES (pH 7.4). Coverslips with the remaining cortices were then submerged in 2% formaldehyde/isotonic buffer for 5 min and processed for immunofluorescence microscopy (Figure 3A).

Microinjections

Dejellied eggs were rowed on coverslips coated with 0.1% protamine sulfate to prevent movement during injections and imaging. Coverslips were mounted in metal injection chambers containing MBLSW maintained at 16C. Injection volumes were set to roughly 3%–5% of the egg volume using a Picospritzer III pressure regulator connected to a foot pedal injection control system. This injection volume resulted in final concentrations of roughly 10.5-17.5 nM of Tau-mCherry, 0.1mg/ml of EB1-GFP, and 0.25 ug/ml of p150-CC1. 20-25 eggs were injected per experiment. Eggs were then allowed to incubate for 10 minutes at 16C to recover from injections. We then fertilized the eggs under the Ziess 880 LSM Airyscan and monitored them for sperm entry and aster growth.

Pharmacological inhibitors

For HG and urethane experiments (Figure 2), inhibitors were added to unfertilized eggs in filtered sea water and pre-incubated for 5-10 minutes before fertilization. Urethane (Sigma, > 99% purity) was diluted in DMSO, and used at a 100 mM final concentration. HG (Sigma) was diluted to 0.7% in MBLSW. Control samples were treated with equal amounts of DMSO to experimental conditions. Ciliobrevin D (Sigma) was diluted to various concentrations in DMSO and added to zygotes 5 minutes post-fertilization (Figure 4A). Zygotes were either fixed ~3-5 minutes later and processed for immunofluorescence microscopy or immediately imaged for live-cell observation of aster dynamics.

Egg nuclear sedimentation and enucleation

Eggs in MBLSW were distributed over a 1.1M sucrose pad at 1 part eggs and 2 parts sucrose (Harvey, 1933). To float the female pronucleus to the egg periphery, we centrifuged them at 10,000 g for 6 minutes. For enucleation, we centrifuged eggs at 10,000 g for 10 minutes. In all conditions we used a Sorval HB-4 rotor. The eggs were then collected, rinsed 2X in filtered sea water, and labeled for DNA using 1ug/ml of Hoescht. We incubated eggs in 100 uM urethane or equal amounts of DMSO for control and enucleated conditions. Following treatment, we fertilized the eggs in glass bottom Petri dishes (35 × 10 mm) and looked for zygotes in which the sperm entered directly opposite of the female pronucleus. We acquired 20-40 um z stacks every 5-15 s until centration and pronuclear fusion was complete.

Chemical ablations

Eggs injected with Tau-mCherry fusion protein were treated with 50 nM of combretastatin 4A (CA4) (a gift from the Mitchison Lab) (Wühr et al., 2010), protected from light, and fertilized 10 minutes after injection. The drug was activated in a defined region of the rear portion, side or front portions of the aster using a 405 nm laser with 13 μsec dwell time on a Zeiss 880 LSM Airyscan. The region of CA4 activation was near the distal portions of MTs (seen by Tau-mCherry signal), to prevent immediate diffusion of the active drug to other portions of the aster. Additionally, eggs in which CA4 was not uncaged were allowed to proceed through spindle formation and cleavage. These samples were subsequently imaged at a Z-plane through the bipolar MTOCs in order to show the center of spindle and telophase asters along their long axis respectively (Figure 5D).

QUANTIFICATION AND STATISTICAL ANALYSIS

All statistical analysis performed in this study were performed using Graphpad Prism 8. The statistical analysis used for each experiment can be found in the corresponding figure legends. The sample sizes (n) represents the number of zygotes used for each experiment and is indicated in each corresponding figure legend. The total n for each experiment in this study is pooled from a minimum of three individual females. All quantifications presented in this study are displayed as averages, and variation is represented as the standard deviation, unless otherwise noted in the figure legend.